

Computational Fluid Dynamics Modeling of Sequential Multimaterial Extrusion Additive Manufacturing

Daniel Helmuth Meile, Carl Emil Hansen Thor, Yohan Jacquet, Md Tusher Mollah, Berin
Šeta, Jon Spangenberg

Department of Civil and Mechanical Engineering, Technical University of Denmark, 2800
Kgs. Lyngby, Denmark

Abstract

Integrating multiple materials into extrusion-based additive manufacturing enables novel fabrication techniques and significantly expands the design freedom of the printed parts. However, multi-material extrusion remains a non-trivial task to implement, particularly due to the complex rheological behavior of the materials involved, influencing both the geometrical accuracy of the printed strand and the hardware requirements of the printing setup. A novel computational fluid dynamics (CFD) model has been developed, for simulating the dynamics of multiple material flows with differing rheological properties. Specifically, a scalar advection approach is used to modulate the rheology of the fluids during the extrusion and deposition of layers. To quantify and control the rheological difference between materials, a dimensionless number Y_{RR} representing the yield stress reduction ratio is introduced. This parameter enables systematic variation of yield stress between materials and serves as a critical factor in assessing interfacial deformation and print stability. The study investigates strand morphology and the dynamics of material switching, offering insights into how rheological mismatch and process parameters affect multi-material deposition. Overall, it provides a digital tool to better understand and optimize the complex flow phenomena inherent to multi-material extrusion additive manufacturing.

Introduction

Material Extrusion Additive Manufacturing (MEX-AM) has demonstrated broad applicability across both industrial and academic settings [1]. An important technique within this field is wet-on-wet printing, where new material layers are deposited before the underlying layers have fully solidified. In the construction industry, the potential of wet-on-wet MEX-AM is exemplified by large-scale 3D Concrete Printing (3DCP), where research groups have successfully fabricated structural components such as pedestrian bridges [2][3]. In materials science, MEX-AM has also been employed to produce high-performance and architected materials, as well as in the manufacturing of advanced composite systems [4].

A major advantage of wet-on-wet MEX-AM compared to other MEX-AM techniques, such as Fused Filament Fabrication (FFF), lies in its enhanced interlayer bonding [5]. This, combined with the capacity to handle high-viscosity and particle-rich mixtures, makes wet-on-wet MEX-AM particularly well suited for Big Area Additive Manufacturing (BAAM). As the field advances toward multi-material extrusion, especially with materials exhibiting significantly different rheological properties, controlling flow behavior and achieving reliable material integration becomes increasingly complex.

Three primary strategies for combining two rheologically distinct fluids in wet-on-wet MEX-AM can be identified:

1. Two-component admixture formulations, where a secondary Newtonian fluid is injected to alter rheology or trigger setting [6].

2. Inline mixing of two non-Newtonian materials, requiring upstream blending via static or dynamic mixers, especially for mineral or clay-based systems [7][8].
3. Deposition of multiple materials, using sequential or simultaneous extrusion to place discrete material regions without mixing, enabling spatial patterning and the creation of functionally graded or architected materials [4][9].

To investigate the complex flow behavior and interfacial dynamics in sequential multi-material extrusion, this study employs a custom-developed CFD model tailored for wet-on-wet MEX-AM. The model captures the sequential extrusion of two rheologically distinct, yield-stress fluids and simulates their deposition under realistic process conditions. A scalar advection technique is used to track material interfaces and modulate viscosity during sequential switching. The simulations aim to resolve internal velocity, shear, and viscosity profiles, providing insights into how rheological contrast and process parameters influence strand morphology, buildability, and stability. This physics-based approach supports the optimization of multi-material printing strategies and material formulations for advanced wet-on-wet MEX-AM applications.

Methodology

In this study, a numerical model was developed to simulate a multi-material-extrusion additive manufacturing (multi-MEX-AM) process. The model was implemented using the commercial CFD software FLOW-3D®, which employs the Split Lagrangian TruVOF® method - an advanced Volume-of-Fluid (VOF) technique designed for precise tracking of free surface flows [10][11]. This makes it particularly well-suited for simulating MEX-AM processes. Assuming incompressible and isothermal flow, the model uses the continuity and momentum equations, discretized with the Finite Volume Method (FVM).

$$\nabla \mathbf{u} = 0 \tag{1}$$

and

$$\rho \left(\frac{\partial \mathbf{u}}{\partial t} + \mathbf{u} \cdot \nabla \mathbf{u} \right) = \rho \mathbf{g} - \nabla p + \nabla \cdot \mathbf{S}_T \tag{2}$$

Where:

- \mathbf{u} is the velocity vector,
- p is the pressure
- t is time
- \mathbf{g} is the gravitational acceleration vector $(0,0,-9.81\text{m/s}^2)$
- \mathbf{S}_T is the deviatoric stress tensor

The deviatoric stress tensor \mathbf{S}_T is calculated using the following generalized Newtonian fluid approach:

$$\mathbf{S}_T = 2 \mu(\dot{\gamma}) \mathbf{D}_T \tag{3}$$

where, μ is the viscosity of the material, $\mathbf{D}_T = (1/2)((\nabla\mathbf{u}) + (\nabla\mathbf{u})^T)$ represents the deformation rate tensor and $\dot{\gamma} = \sqrt{2\text{tr}(\mathbf{D}_T^2)}$ is the strain rate.

The model captures the flow behavior of two non-Newtonian fluids with distinct rheological properties as they are extruded through a dual-channel nozzle (Figure 1A–B). Each channel has an inner diameter of 7.5 mm and merges at a junction located 11.14 mm downstream from the nozzle outlet, measured along the arc length of the connecting path. The nozzle is designed with two separate mass sources: one for Fluid 1, which contains no additional solute, and one for Fluid 2, into which a scalar mass is introduced to represent an additive or solute. Material is introduced into the nozzle only through the lower portion of each mass source, thereby constraining the injection region.

The nozzle translates along the x -axis at a constant velocity of $V = 10$ mm/s, while extruding material at a volumetric flow rate defined by $Q = U\pi r^2$, where U is the extrusion speed and r is the radius of the nozzle outlet. The relationship between the translation speed and extrusion speed is characterized by a dimensionless speed ratio, $S_R = V/U$. Similarly, the ratio between the nozzle outlet diameter and the gap between the nozzle and the substrate is defined as the gap ratio, $G_R = h/D$, where h is the gap height and D is the nozzle outlet diameter.

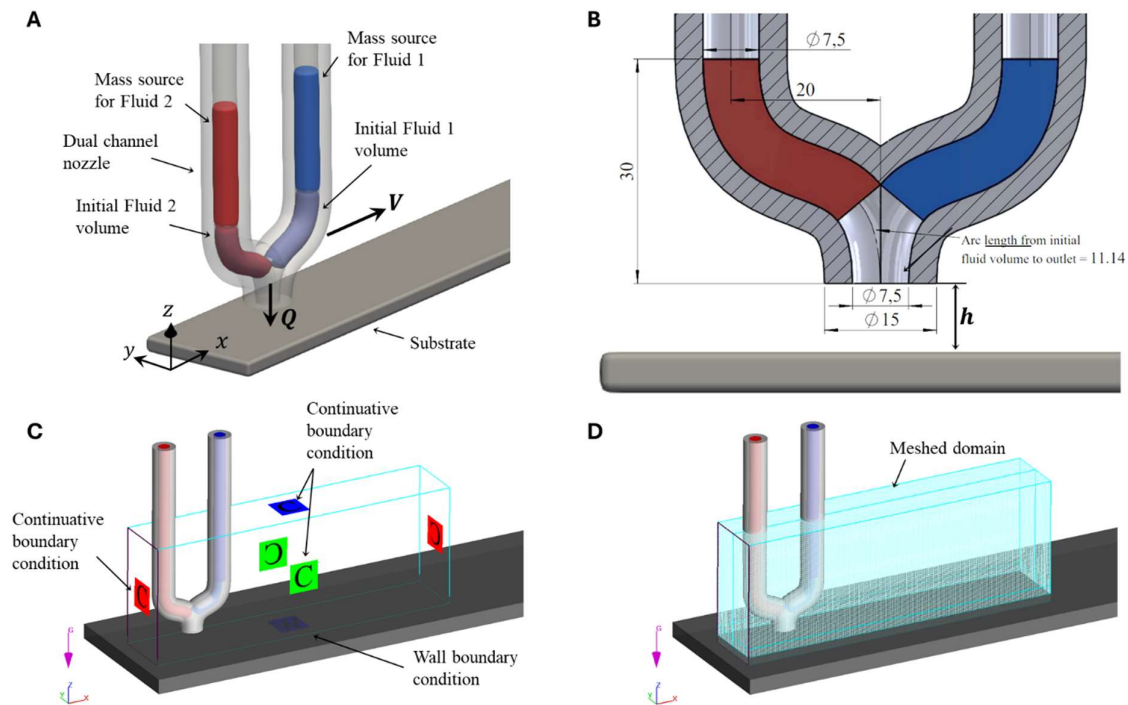


Figure 1: A-B Parameter characterization. C-D CFD model conditions and meshed domain.

The build domain, illustrated in Figure 1C, is subject to specific boundary conditions. Continuative (outflow) boundary conditions are applied to the lateral and top boundaries, allowing material and flow to exit the domain without any constraint, whereas a no-slip wall boundary condition is imposed on the bottom boundary. The boundaries of the solid geometries, i.e., the nozzle and substrate, are also imposed with a no-slip condition. The build volume measures $0.210 \text{ m} \times 0.04 \text{ m} \times 0.08 \text{ m}$ in the x -, y -, and z -directions, respectively. The

domain is discretized using a non-conformal Cartesian grid with a cell size of 1.25 mm, resulting in approximately 344,000 computational cells as seen in Figure 1D.

Rheology

To describe the rheological behavior of the fluids in this study, a Bingham fluid model is employed. The apparent viscosity, denoted by $\mu(\dot{\gamma})$ is defined as:

$$\mu(\dot{\gamma}) = \eta_p + \frac{\tau_c}{\dot{\gamma}} \quad (4)$$

Where:

- η_p is the plastic viscosity fluid
- τ_c is the yield stress of the fluid
- $\dot{\gamma}$ is the shear rate.

This formulation captures the characteristic yield-stress behavior of Bingham fluids. However, as $\dot{\gamma} \rightarrow 0$ the apparent viscosity tends toward infinity, to avoid numerical singularity, a lower bound for the minimum shear rate, $\dot{\gamma}_c$ is introduced. The apparent viscosity is thus regularized using a bi-viscous approach, resulting in:

$$\mu_{app}(\dot{\gamma}) = \begin{cases} \eta_p + \frac{\tau_c}{\dot{\gamma}_c}, & \dot{\gamma} < \dot{\gamma}_c \\ \eta_p + \frac{\tau_c}{\dot{\gamma}}, & \dot{\gamma} \geq \dot{\gamma}_c \end{cases} \quad (5)$$

Note that for shear rates lower than $\dot{\gamma}_c$, a constant maximum apparent viscosity is reached. The choice of $\dot{\gamma}_c$ is made based on the impact on numerical stability and its effect on the final CFD result, which can be determined by performing a sensitivity analysis. For this study, a minimum shear rate of $\dot{\gamma}_c = 0.1 \text{ s}^{-1}$ was used, as smaller values had a negligible impact on the results of the simulation [12] [13].

Viscosity Modification via Scalar Advection

To simulate the effect of a dissolved substance (such as an additive or solute) on the fluid viscosity and yield stress, a scalar mass is introduced into Fluid 2 and treated as an interstitial solute. The viscosity of the resulting mixture is modeled using a weighted mixing rule:

$$\mu_{mix} = \frac{\rho_1 \mu_{app} + S_c \mu_c}{\rho_1 + S_c} \quad (6)$$

Where:

- ρ_1 and μ_{app} is the density and apparent viscosity of Fluid 1, respectively,
- S_c is the scalar mass concentration,
- μ_c is the viscosity attributed to the scalar.

In this study, we assume the viscosity attributed to the scalar is equal to the plastic viscosity of Fluid 1, i.e. $\mu_c = \eta_p$. Furthermore, the scalar mass concentration is set equal to the product of a scalar C and the density of Fluid 1, i.e. $S_c = C\rho_1$. It is important to note that

the addition of the scalar mass to the fluid does not contribute to or alter the fluid's bulk density. Substituting into the mixing rule yields:

$$\mu_{mix} = \frac{\mu_{app} + C\eta_p}{(1 + C)} \quad (7)$$

A simplification of equation (7) is possible, as the apparent viscosity of Fluid 1 is given as a function of the shear rate in equation (4), which yields

$$\mu_{mix} = \frac{\eta_p + \frac{\tau_c}{\dot{\gamma}} + C\eta_p}{(1 + C)} = \eta_p + \frac{\tau_c}{(1 + C)\dot{\gamma}} \quad (8)$$

Rearranging gives:

$$\mu_{mix} = \eta_p + \frac{\tau_c \cdot Y_{RR}}{\dot{\gamma}} \quad (9)$$

Here, we define Y_{RR} , which will be referred to as the yield stress reduction ratio.

$$Y_{RR} = \frac{1}{1 + C} \quad (10)$$

This interpolates the influence of the scalar on the effective yield stress, with the limits:

- $Y_{RR} \rightarrow 1$ as $C \rightarrow 0$ (no scalar added),
- $Y_{RR} \rightarrow 0$ as $C \rightarrow \infty$ (scalar added).

From this, it is also clear that the Y_{RR} can only reduce the yield stress of the fluid in which the scalar mass is dissolved. We further define the Y_{RR} in terms of the yield stresses in the two fluids:

$$Y_{RR} = \frac{\tau_{c2}}{\tau_{c1}} \quad (11)$$

Where τ_{c1} and τ_{c2} are the yield stresses for Fluid 1 and Fluid 2, respectively. Given the relationship, the scalar mass concentration required to achieve a specific yield stress in Fluid 2 can then be expressed as:

$$S_c = \left(\frac{\tau_{c1}}{\tau_{c2}} - 1 \right) \cdot \rho_1 \quad (12)$$

This formulation enables controlled reduction of the fluid's yield stress through scalar addition while preserving a consistent mathematical structure compatible with the Bingham fluid model. Therefore, equation (6) presenting the mixture viscosity is used in the equation (3), i.e., μ_{mix} is used instead of μ when evaluating the viscosity of Fluid 2. Moreover, the above scalar approach identifies Fluid 1 and Fluid 2 during the printing process and alters the viscosity of the material accordingly. This study places special emphasis on cementitious materials, hereby utilizing the specific properties listed in Table 1.

Table 1: Rheological parameters used for CFD modelling [13] [14]

Parameter	Value	Symbol
Density	2100 kg. m ⁻³	ρ_1
Plastic viscosity	7.5 Pa. s	η_p
Yield stress	630 Pa	τ_{c1}
Critical shear rate	0.1 s ⁻¹	$\dot{\gamma}_c$

Toolpath and extrusion strategy

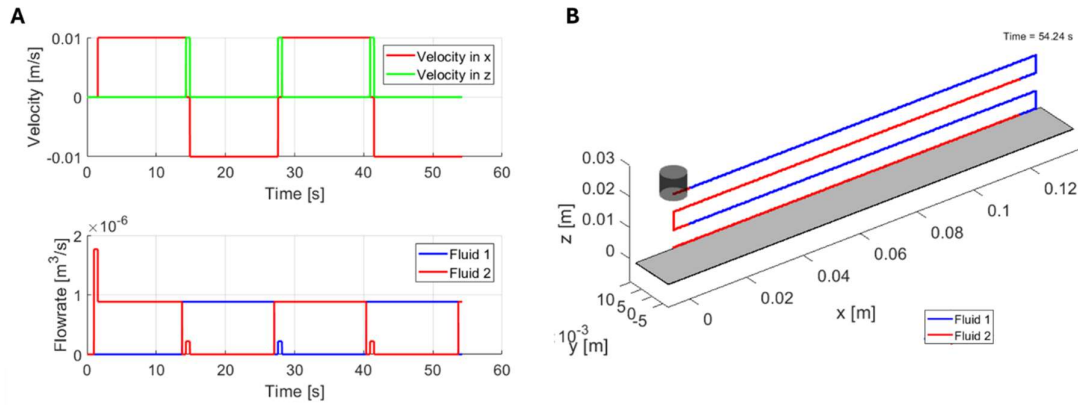


Figure 2: A. Velocity of nozzle and flowrates of mass sources over time. B. Resulting toolpath and extrusion strategy.

To provide the necessary input for the CFD simulation, including nozzle motion and mass source flowrates, a custom MATLAB script was developed. This script generates velocity and flowrate arrays, as seen in Figure 2A, and exports them as .csv files compatible with FLOW-3D®. By integrating the velocity arrays over time, a corresponding toolpath is constructed, consisting of four stacked layers with a layer height of $h = 5.625$ mm (gap ratio, $G_R = 0.75$), as shown in Figure 2B. The extrusion strategy is synchronized with the toolpath to produce an alternating material deposition pattern. The material switching is intentionally triggered early, as switching materials at the exact nozzle position would cause a delay in fluid delivery, leading to misalignment between the intended and actual material deposition locations. This early extrusion is determined by the nozzle geometry (as shown in Figure 1B) to account for the residual material volume in the merging zone, located 11.14 mm downstream from the nozzle outlet. Specifically, this zone contains approximately 500 mm³ of Fluid 1, which must be extruded before Fluid 2 can reach and exit the nozzle. The time used to apply the early offset in the extrusion strategy is calculated as $t_{early} = 11.14 \text{ mm}/U$, where U is the extrusion speed.

Results & Discussion

Figure 3A presents the theoretical relationships between shear rate and both the dynamic viscosity and shear stress for the Bingham fluid model applied to Fluid 1 and Fluid 2, with a $Y_{RR} = 0.5$. As expected, the apparent viscosity decreases with increasing shear, while shear stress increases linearly beyond the yield point - a characteristic of Bingham fluids. These theoretical trends provide a baseline for interpreting the simulation results.

Figure 3B shows a cross-sectional (XZ-plane) view of the CFD simulation during the deposition of the fourth layer, illustrating the spatial distribution of dynamic viscosity within the printed structure. The pattern aligns with the shear-dependent behavior described in Figure 3A: regions subjected to high shear, such as near the nozzle outlet and at layer interfaces, display reduced viscosity, while areas with minimal flow retain higher viscosity due to yield stress effects. This consistency between simulation output and theoretical predictions confirms the implementation of the Bingham rheology in the CFD model.

Further examination of Figure 3B reveals how the rheological properties of Fluids 1 and 2 evolve throughout the 3D printing process. The first two layers achieve maximum apparent viscosities of approximately 3150 Pa.s for Fluid 2 (first layer), consistent with a Y_{RR} of 0.5 while approximately 6300 Pa.s for Fluid 1 (second layer). This behavior extends into the third layer, except in the region directly below the nozzle outlet, where the extrusion causes a local viscosity reduction, by nearly a factor of two, across approximately half the layer's thickness.

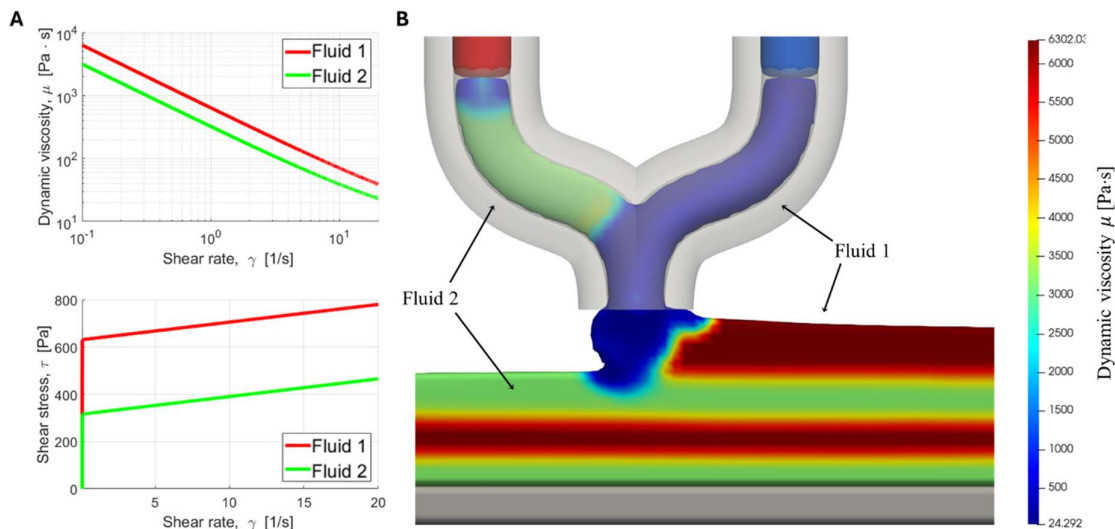


Figure 3: A. Theoretical calculations B. CFD model results

In the fourth and top layer, two distinct zones are observed. One zone, composed of Fluid 1, maintains a steady-state viscosity near 6300 Pa.s, corresponding to a shear rate of approximately 0.1 s^{-1} . The second zone, located below the nozzle, exhibits a more complex viscosity profile, with values falling below 1000 Pa.s, indicating localized shear rates exceeding 5 s^{-1} . The transition between these high and low shear rate regions, marked by a dynamic viscosity around 2500 Pa.s, spans roughly 15 mm, about twice the nozzle diameter, and aligns with observations reported in prior studies[15].

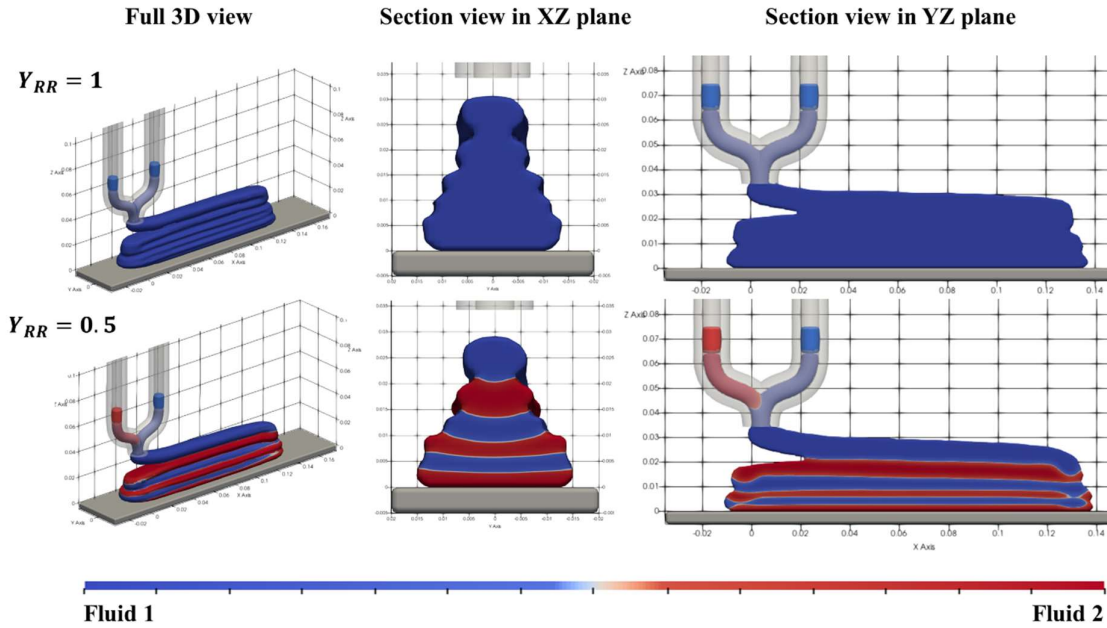


Figure 4: Single material ($Y_{RR} = 1$) vs. multi-material print ($Y_{RR} = 0.5$)

To assess the impact of the yield stress reduction ratio, Y_{RR} , on the structural integrity of a 3D printed structure, two simulations were performed using the same extrusion strategy described earlier, with the only difference being the use of six layers instead of four. The first simulation employed a single-material system, e.g. $Y_{RR} = 1$, while the second used a multi-material configuration, e.g. $Y_{RR} = 0.5$, indicating that the yield stress of Fluid 2 (in red) is half that of Fluid 1 (in blue).

Figure 4 compares the two printing scenarios and illustrates the influence of decreasing the yield stress of Fluid 2 relative to Fluid 1. At lower Y_{RR} , the reduced yield stress of Fluid 2 results in greater lateral spreading under the load of subsequent layers. This compromises the structural integrity of the print, leading to reduced height and partial collapse.

As the nozzle continues along the predefined tool path, the gap ratio G_R , effectively increases due to the sinking of underlying layers. This, combined with the mismatch in rheological properties, induces stress concentrations within the material, as the deposited layers become narrower. These localized stresses cause the more viscous Fluid 1 to intrude into the center of the deformed Fluid 2 layer, displacing the less viscous material outward and further altering the strand geometry.

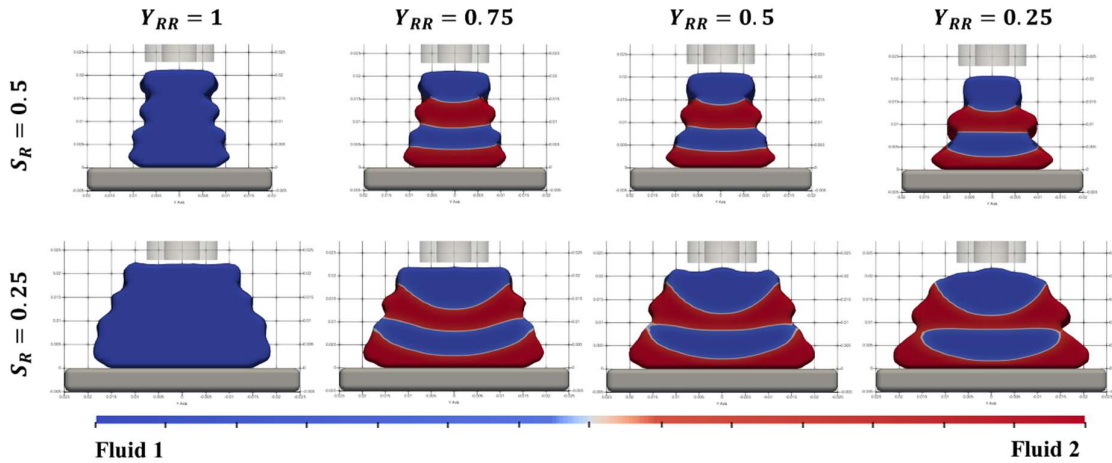


Figure 5: Influence of Y_{RR} and S_R on the strand morphology of a resulting geometry

Figure 5 illustrates the impact of Y_{RR} and S_R on the resulting geometry of a four-layer printed structure. The speed ratio is defined as the ratio of nozzle translation speed to the velocity of the extruded material and serves as a critical parameter controlling both layer height and lateral spreading.

At lower S_R , more material is deposited per unit length of travel, resulting in thicker layers and increased lateral expansion. This effect leads to greater deviations in top-layer width compared to high-speed ratio cases. In this regime, extrusion pressure, which depends on the flow rate Q and the gap height h , becomes the dominant force driving material deformation. As a result, Fluid 1, forming the upper layers, exhibits enhanced spreading behavior due to reduced confinement.

In contrast, higher S_R lead to thinner layers in the lateral direction due to a reduced material deposition rate. Under these conditions, extrusion pressure no longer dominates the deformation behavior; instead, gravitational forces become the primary driver. As a result, the pressure exerted by the overlying Fluid 1 layers is distributed more uniformly across the width of the strand, producing a more horizontal interface between Fluid 1 and Fluid 2. In this regime, the response of Fluid 2 becomes increasingly sensitive to rheological mismatch. As the Y_{RR} decreases (i.e., as Fluid 2 becomes less resistant to deformation compared to Fluid 1), the bottom layer experiences greater compression under the applied load. This squeezing effect is most pronounced in the first layer directly beneath Fluid 1, highlighting the critical role of rheological differences in governing the interaction between layers.

An extreme case ($Y_{RR} = 0.25$ & $S_R = 0.5$) arises when the top layer N retains a width close to the nozzle's internal diameter. In this case, the upper layer undergoes minimal lateral spreading, concentrating the extrusion pressure onto the underlying layer $N - 1$. This concentrated stress causes Fluid 2 to laterally spread, producing a geometry nearly identical to that of the layer $N - 2$.

When both Y_{RR} and S_R are low, the interaction becomes particularly unstable. The flow conditions promote excessive lateral spreading and can lead to over-molding of Fluid 1 onto the lower layers, compromising structural definition and interlayer fidelity.

Proof of concept

To demonstrate the capabilities of wet-on-wet multi-MEX-AM, a proof-of-concept simulation was conducted to evaluate the precision of switching between two fluids with distinct rheological properties. For this case, a $Y_{RR} = 0.75$ was used to reduce the yield stress of Fluid 2. As illustrated in Figure 6A, a six-layer toolpath incorporating the letters "SFF" using the printing parameters $G_R = 0.75$ and $S_R = 0.5$, was prepared to assess the spatial resolution and control of the multi-material deposition. To ensure accurate material placement, the previously discussed early extrusion offset, t_{early} , was applied, resulting in the adjusted strategy shown in Figure 6B. Simulating this toolpath and extrusion strategy, using the developed CFD model, successfully reproduced the intended letter pattern with clear legibility, as seen in Figure 6C.

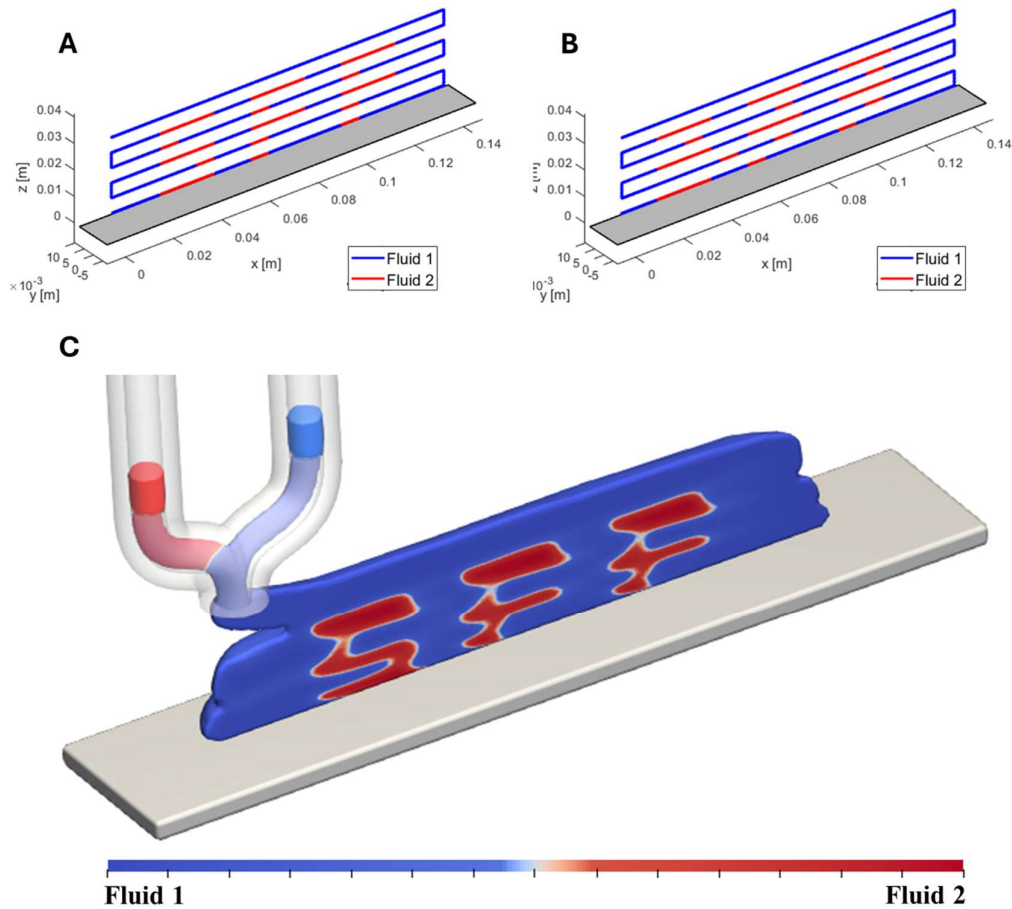


Figure 6: A. Toolpath and Extrusion strategy without early extrusion offset, B. Toolpath and Extrusion strategy with early extrusion offset, C. CFD result containing Fluid 1 & Fluid 2

From Figure 6C it can be observed that the deposited fluids exhibit minimal misalignment from their intended spatial positions, confirming the effectiveness of the early extrusion offset strategy in compensating for the residual material volume in the nozzle. Furthermore, the interface between Fluid 1 and Fluid 2 within individual strands appears inclined, introducing a slight angular deviation from the idealized geometry. This suggests that while the overall material placement is well-controlled, the internal interface dynamics remain sensitive to transient flow conditions during material switching.

Conclusion

This work establishes a CFD model to simulate and optimize sequential multi-material extrusion using Bingham fluids in wet-on-wet MEX-AM. By implementing a scalar-based viscosity modulation scheme with Bingham rheology, the model captures critical flow dynamics during material switching and deposition. Simulation results reveal that the yield stress reduction ratio, Y_{RR} , has a pronounced impact on strand morphology, stability, and overall buildability. The study further demonstrates that the printed part geometry is influenced not only by the Y_{RR} , but also by its interaction with the speed ratio S_R . The coupling of these parameters significantly affects material deposition behavior, indicating that both rheological properties and printing parameters must be jointly considered to achieve optimal print quality. Low Y_{RR} values reduce structural integrity by increasing lateral deformation, while low S_R values intensify material spreading and amplify rheological mismatches between layers. Conversely, high S_R values mitigate these effects but introduce interfacial squeezing and stress concentration.

The model's ability to reproduce complex deposition patterns, as demonstrated in the 'SFF' proof-of-concept, highlights its utility for predicting and optimizing multi-material printing strategies. The framework developed in this study provides a robust basis for exploring advanced printing techniques, including functionally graded materials and rheology-tailored formulations. Future work will involve experimental validation using the dual-channel nozzle to fabricate the simulated structures.

Acknowledgements

The authors would like to express their gratitude to Innovation Fund Denmark (Grant no. 0223–00084B), as well as FLOW-3D®, for their support in providing software licenses.

References

- [1] V. Mechtcherine, V.N. Nerella, F. Will, M. Näther, J. Otto, M. Krause, Large-scale digital concrete construction – CONPrint3D concept for on-site, monolithic 3D-printing, *Automation in Construction* 107 (2019) 102933. <https://doi.org/10.1016/j.autcon.2019.102933>.
- [2] A. Dell'Endice, S. Bouten, T. Van Mele, P. Block, Structural design and engineering of Striatus, an unreinforced 3D-concrete-printed masonry arch bridge, *Engineering Structures* 292 (2023) 116534. <https://doi.org/10.1016/j.engstruct.2023.116534>.
- [3] Z. Ahmed, R. Wolfs, F. Bos, T. Salet, A Framework for Large-Scale Structural Applications of 3D Printed Concrete: the Case of a 29 m Bridge in the Netherlands, *Open Conf Proc* 1 (2022) 5–19. <https://doi.org/10.52825/ocp.v1i.74>.
- [4] N.M. Larson, J. Mueller, A. Chortos, Z.S. Davidson, D.R. Clarke, J.A. Lewis, Rotational multimaterial printing of filaments with subvoxel control, *Nature* 613 (2023) 682–688. <https://doi.org/10.1038/s41586-022-05490-7>.
- [5] Interlayer Mechanical Properties of Thermoset Components Produced by Material Extrusion Additive Manufacturing - DTU Findit, (n.d.). <https://findit.dtu.dk/en/catalog/67ee8673be618a12f3e76ac9> (accessed June 23, 2025).
- [6] T. Wangler, Y. Tao, A. Das, M. Mahmoudi, S. Gürel, R.J. Flatt, Aluminate 2K systems in digital concrete: Process, design, chemistry, and outlook, *Cement and Concrete Research* 185 (2024) 107644. <https://doi.org/10.1016/j.cemconres.2024.107644>.
- [7] Y. Tao, A.V. Rahul, K. Lesage, Y. Yuan, K. Van Tittelboom, G. De Schutter, Stiffening control of cement-based materials using accelerators in inline mixing processes:

- Possibilities and challenges, *Cement and Concrete Composites* 119 (2021) 103972. <https://doi.org/10.1016/j.cemconcomp.2021.103972>.
- [8] A. Deetman, D. Bos, J. Blaakmeer, T. Salet, S. Lucas, An in-line dye tracer experiment to measure the residence time in continuous concrete processing, *Mater Struct* 57 (2024) 104. <https://doi.org/10.1617/s11527-024-02378-y>.
- [9] M.A. Skylar-Scott, J. Mueller, C.W. Visser, J.A. Lewis, Voxelated soft matter via multimaterial multinozzle 3D printing, *Nature* 575 (2019) 330–335. <https://doi.org/10.1038/s41586-019-1736-8>.
- [10] C.W. Hirt, B.D. Nichols, Volume of fluid (VOF) method for the dynamics of free boundaries, *Journal of Computational Physics* 39 (1981) 201–225. [https://doi.org/10.1016/0021-9991\(81\)90145-5](https://doi.org/10.1016/0021-9991(81)90145-5).
- [11] R. Comminal, J. Spangenberg, Three-dimensional cellwise conservative unsplit geometric VOF schemes, *Journal of Computational Physics* 442 (2021) 110479. <https://doi.org/10.1016/j.jcp.2021.110479>.
- [12] M.T. Mollah, R. Comminal, M.P. Serdeczny, B. Šeta, J. Spangenberg, Computational analysis of yield stress buildup and stability of deposited layers in material extrusion additive manufacturing, *Additive Manufacturing* 71 (2023) 103605. <https://doi.org/10.1016/j.addma.2023.103605>.
- [13] M.T. Mollah, R. Comminal, M.P. Serdeczny, D.B. Pedersen, J. Spangenberg, Stability and deformations of deposited layers in material extrusion additive manufacturing, *Additive Manufacturing* 46 (2021) 102193. <https://doi.org/10.1016/j.addma.2021.102193>.
- [14] R. Comminal, W.R. Leal Da Silva, T.J. Andersen, H. Stang, J. Spangenberg, Modelling of 3D concrete printing based on computational fluid dynamics, *Cement and Concrete Research* 138 (2020) 106256. <https://doi.org/10.1016/j.cemconres.2020.106256>.
- [15] M.T. Mollah, R. Comminal, M.P. Serdeczny, D.B. Pedersen, J. Spangenberg, Numerical Predictions of Bottom Layer Stability in Material Extrusion Additive Manufacturing, *JOM* 74 (2022) 1096–1101. <https://doi.org/10.1007/s11837-021-05035-9>.